AIAA JOURNAL
Vol. 61, No. 12, December 2023

High-Frequency Pulsed Coaxial Injectors for High-Speed Flow Mixing and Control

John T. Solomon,* Rhys Lockyer,† and Tailor Jones†
Tuskegee University, Tuskegee, Alabama 36088
and
Phillip Kreth‡
University of Tennessee Space Institute, Tullahoma, Tennessee 37388

https://doi.org/10.2514/1.J062369

Efficient and controlled mixing of fuel with fast-moving air is a challenging physical problem relevant to hypersonic systems. Although mixing happens at the molecular level through diffusion, the macroscopic phenomenon such as entrainment and vorticity dynamics resulting from the shear layer instabilities of the mixing fluids play a significant role in the overall efficiency of the process. With a focus on improving mixing at extreme flow conditions, this paper presents a fundamental study of a novel, high-speed, pulsed coflow system integrated with ultrahigh-frequency actuators (11–20 kHz). This injection system consists of a supersonic actuation air jet at the inner core that provides large mean and fluctuating velocity profiles in the shear layers of a fluid stream injected surrounding the core through an annular nozzle, with pulsing occurring at a designated frequency. The high-frequency streamwise vortices and shockwaves tailored to the mean flow significantly enhanced supersonic flow mixing between the fluids compared to a steady coaxial configuration operating at the same input pressure. Experiments also indicate a strong connection between the frequency and unsteady amplitude of the actuation jet to the supersonic flow mixing phenomenon. This paper reports the design details of the injector assembly and flow mixing characteristics captured using phase-locked microschlieren and planar laser-induced fluorescence techniques.

I. Introduction

THE efficient mixing of two fast-moving fluid streams is a crucial engineering problem in high-speed combustion systems. Several aerospace applications use a coaxial jet configuration, a simple and effective mixing method in which fluids flowing separately through the inner core and the annular space meet at the exit plane of the nozzle assembly. For example, in applications like a gas turbine or combustion chamber of a rocket engine, these fluids could be oxidizers, such as gaseous or liquid oxygen, and fuel in its liquid or gaseous phase. Effective and controlled mixing can lead to higher combustion efficacy, longer life, reduced combustor size, stable operations, and fewer emissions/pollutants. Although the mixing ultimately happens at the molecular level, active flow control techniques can tailor the flow dynamics at micro- and macro-scales in favor of rapid diffusion at the molecular level [1–3].

The microscopic convective time scale (order of milliseconds) associated with hypersonic flow systems demands effective fuel injection techniques for their efficient and stable operations. There is a need for robust flow control actuators to enhance microscale mixing at high-speed and positively alter the macroscopic phenomenon involved. The entrainment and vorticity dynamics resulting from the shear layer instability modification play a significant role in the overall efficiency of the mixing process. Since the flow mixing problem and control face more challenges at extreme flow conditions, feasible solutions are critical to advancing next-generation airbreathing hypersonic flight systems at the forefront of national priorities defense. Passive methods proposed for improved mixing use flush-mounted or intrusive injectors to generate streamwise, counter-rotating vortices for rapid nearfield mixing of the incoming air and fuel [4–12]. Beyond the classical passive coaxial configuration, a few studies explore active schemes such as powered resonance tubes or Hartmann–Sprenger tubes as an option to excite the shear layer at high frequency [13]. Studies show that such active jet modulation is promising for improving penetration and high-speed mixing compared to unmodulated jets. However, the limited operational bandwidth and larger size restrict their implementation in practical systems.

The current paper presents the design and experimental studies on an active coaxial injector configuration, as shown in Fig. 1. This design could tailor the instabilities of an injected coflowing fluid using a pulsed supersonic air jet blasting up to 20 kHz with a bandwidth of 10 kHz. The injector assembly shown in Fig. 1 has four major components: 1) an underexpanded source jet from a steel tube of 1.5 mm diameter enters 2) an injector assembly made of three plates with internal cavities fabricated with the desired cavity volume of 20.3 mm^3, and 3) another steel tube (1 mm inner diameter [ID], 1.5 mm outer diameter [OD]) that allows pulsed jet flows out of the cavities, and 4) a separate fluid passage that opens up around the 1 mm steel tube through a circular orifice of 1.95 mm diameter forming an annular space at the exit of the assembly. This annular space forms a circular slit with a 1.5 mm radius and a thickness of 230 μm, as indicated in Fig. 1. This coaxial annular orifice injects a steady fluid stream while the central steel tube exits a pulsed actuation air jet. Both fluids meet coaxially at the exit plane of the assembly, as shown in Fig 1. The first three components shown in Fig. 1 (i.e., an underexpanded steady jet, a cavity that forms the boundaries for fluid resonance phenomenon, and the pulsed jet that flows out from the cavity, which is called resonance-enhanced microjet [REM]) constitute the actuator system that is integrated to the coaxial injector assembly. Solomon et al. have extensively researched REM actuators and suggested a semi-empirical design correlation that can predict the pulsing frequency [14].

The most crucial parameter that defines the resonance frequency is the cavity volume V. The nozzle pressure ratio of the source jet (NPR), the distance of the cavity from the source jet nozzle entrance (h), the diameter of the source nozzle (d), and the area ratio (ratio of the inlet to the outlet flow area of the cavity) are the other key parameters that affect the resonance phenomenon and its frequency response. These parameters essentially decide the mass flow to the

Presented as Paper 2022-3926 at the 47th AIAA Aviation Forum, Chicago, IL, June 27–July 1, 2022; received 23 August 2022; revision received 31 July 2023; accepted for publication 2 August 2023; published online 25 August 2023.

*Professor, Department of Mechanical Engineering; jsolomon@tuskegee.edu. Senior Member AIAA (Corresponding Author).
†Research Assistant.
‡Assistant Professor, Department of Mechanical, Aerospace, and Biomedical Engineering. Senior Member AIAA.

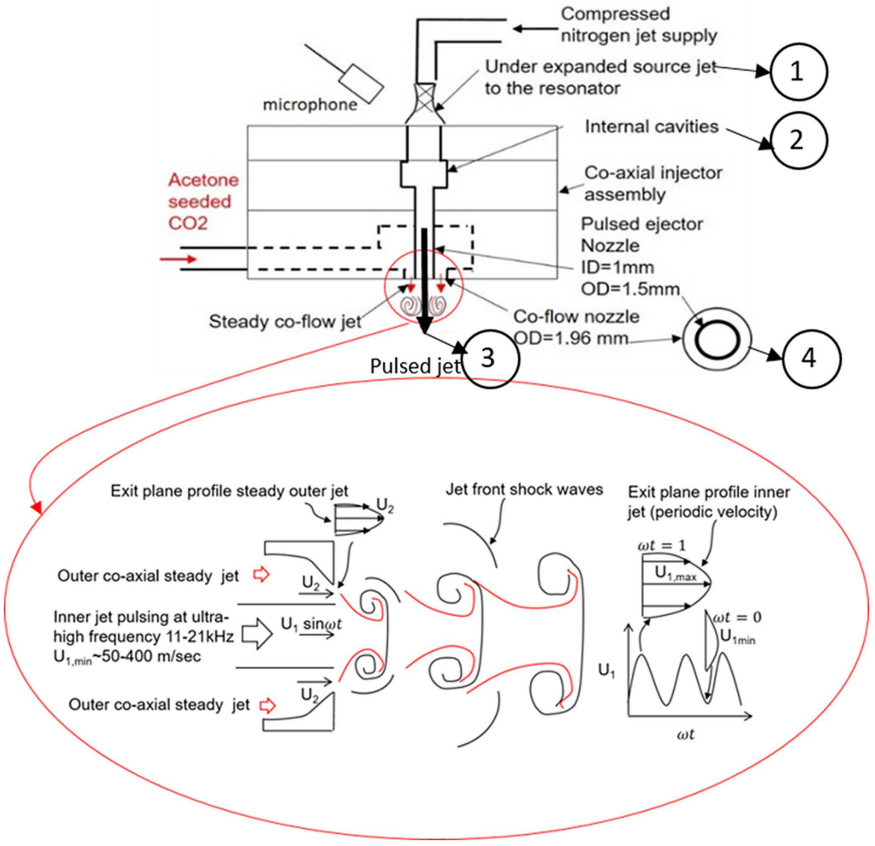

Fig. 1 Schematic of the pulsed coaxial injector assembly and the four major elements.

cavity, boundary conditions for resonance, and net mass accumulation within the cavity. Studies by Uzun et al. [15], who have numerically simulated the REM actuator system, provide significant insights into the flow physics of the resonance phenomenon. The underexpanded source jet essentially "fills up" the cavity as the net mass flow rate (inflow–outflow) is designed to be positive, leading to its pressurization while the REM jet flows outside. The cavity pressure rises to an equilibrium static pressure value; the limit is decided by the degree of underexpansion of the source jet. The increased cavity pressure resists inflow by normal and oblique shock formation at the cavity entrance that diverts the source flow outside ("spilling phase"). The diverted flow causes pressure relief within the cavity as the REM jet still flows out of it. This low pressure allows the source jet to flow again into the cavity, and this cycle repeats itself, causing large pressure fluctuations, driving the REM flow from the cavity in a pulsing mode. It is important to note that an underexpanded source jet (element 1 in Fig. 1) is essential for the resonance phenomenon. The resonance phenomenon trigger only for a range of NPR = 4.0–6.8 (nozzle pressure ratio) of the source jet. The source jet is highly underexpanded at this pressure, with periodic shock cells in the jet core. Due to the presence of shock cells, the static pressure of the jet at the centerline varies periodically in the axial direction, which is responsible for boundary conditions essential for the "filling and spilling" phenomenon, pressure fluctuations inside the cavity, and pulsed REM actuator jet output from the cavity. Under suitable geometric and flow conditions, such a design can generate unsteady supersonic jets over a large bandwidth of 1–60 kHz. Various REM actuator designs and their implementations into several high-speed flow control applications are available in Solomon et al. [14–19].

Figure 1 also shows representative flow patterns of the flowfield at the exit of the nozzle assembly when the steady coaxial jet interacts with the central actuation jet. The inner jet velocity U_1 has a periodic variation from ~10 to 400 m/s, generating a highly unsteady velocity profile at the exit, as indicated in Fig. 1. The coaxial annular stream exit with a constant velocity of U_2 that depends on the injection pressure. Its shear layer is exposed to ambient air and the central pulsing jet on the other side. Section II discusses more design details of the coaxial injector assembly and the mechanism of generating the ultrasonic, supersonic pulsed jet.

The actuation jet exiting the nozzle assembly generates high-frequency pulsed compressible vortices and shockwaves. The fluid injected through the outer core will get entrained into this fast-moving vortex and diffuses into it as it travels downstream. These vortices and shockwaves excite the shear layer of annular flow on micro- and macroscales, causing enhanced mixing between them. The ongoing work aims to understand the flow dynamics of this pulsed coaxial assembly using specially designed phase-locked microschlieren imaging and quantitative measurements using planar laser-induced fluorescence (PLIF). PLIF is a noninvasive measurement technique. It is suitable for quantifying the mixing characteristics of acetone-seeded annular jets that interact with high-frequency pulsed actuation air-jet and air in the surrounding ambiance.

The PLIF method used in this study uses a thin laser sheet of 266 nm wavelength to fluoresce the absorbing species (acetone) in a given measurement volume. Many studies report that acetone fluorescence has a linear variation with concentration and laser power [20,21]. Acetone absorbs ultraviolet light (225–320 nm) but fluoresces in blue (350–550 nm). This study uses CO_2 as an annular stream and compressed nitrogen for generating high-frequency actuator jet pulses. Since the resulting fluorescence is proportional to the amount of the absorbing species in the measurement volume, measuring the intensity of light from the fluorescent molecules captured using an appropriate camera with a filter will quantify the mixing. The mixture fraction calculated at each location usually represents the mixing characteristics of the flow.

II. Experimental Details

A. Facility Description

1. *Microschlieren System*

The experiments presented in this paper were conducted in the microscale flow diagnostic laboratory at Tuskegee University with

support from the U.S. National Science Foundation. The experimental setup consists of a vibration-free optical table with state-of-the-art data acquisition and flow-imaging systems, as shown in Fig. 2. Figure 3 shows a photograph of the experiment setup with all components marked. Note that the actuator jets were oriented horizontally in all experiments to avoid interactions with the optical bench.

The phase-locked microschlieren image acquisition uses a Photron mini™ high-speed camera. This monochromatic camera captures up to 4000 frames per second at its full resolution of 1280×1024 pixels. A lens-based microschlieren system shown in Fig. 3 has been set up on the optical table to visualize the active nozzle's microscale supersonic flowfield. The light source in this microschlieren system uses a custom-made LED and circuit that provides white light with a pulse width of 80 ns. Such a light source with an extremely short pulse duration allows "freezing" and capturing the high-speed microscale compressible flow structures generated by the active nozzle assembly.

In the microschlieren system, a light from the LED is focused onto a sharp rectangular aperture using a condensing lens. A 60 mm lens collimates, and another focuses this beam to the edge of a sharp knife and cuts the image intensity to half. A camera lens positioned at an appropriate distance captures the image of the flowfield kept in test section 5, as indicated in Fig. 3. The pulsing frequency of the actuator is measured using a Grass microphone. Another microphone (B&K) with an amplifier generates signals for phase-locked measurements. This signal goes to an SR645 dual-pass filter before generating frequency-divided, pulsed square waves CD and AB using a DG 645 delay generator with an appropriate delay between the pulses. These signals trigger the camera and the LED light source for phase-locked measurements. A high-pressure compressed nitrogen tank (2000 psi) supplies air to the source jet nozzle coupled to the pulsed jet injector assembly. Compressed CO_2 gas was used as the coaxial stream for microschlieren flow visualization studies. A multichannel oscilloscope monitors all signals used for measurements for accuracy.

2. *Setup for Planar Laser-Induced Fluorescence*

The PLIF imaging uses a setup established at Tuskegee University, as shown in Fig. 4. The critical component of this setup is a Quantel EverGreen™ Nd-YAG dual-pulsed laser with a choice of pulse energies up to 200 mJ at 532 nm and 30 mJ at 266 nm with a repetition rate of 15 Hz. PLIF experiments use laser pulses at 266 nm. A Powerview™ LS-LCD camera (29 MP, 6600×4400), with high quantum efficiency, low noise with 1.8 frames/s, selectable 12-bit or 14-bit output, and 100 mm f/2.8 camera lens, acquires the images. An eight-channel digital laser pulse synchronizer with 250 ps resolution controls the laser pulses and the trigger for the camera. A UV optic periscope and adjustable laser sheet optics (LSO) with 266/532 mm AR (Anti-Reflective) coat create a thin laser sheet at an appropriate test plane in the flowfield generated by the pulsed coaxial assembly. A six-jet oil droplet generator creates saturated acetone vapor in CO_2 gas, the seed fluid stream used for mixing experiments. The image acquisition and analysis use INSIGHT4G™ software. Figure 4b shows a photograph of the PLIF imaging setup established for this study.

3. *Measurement of Nearfield Spectra of Actuator Flowfield*

The unsteady spectra of the flowfield of the active nozzle assembly were measured using a GRAS™ 1/4-inch Free-Field Microphone with a sensitivity of 4 mV/Pa. National Instruments™ 9234, 24-bit, 51.2 kHz data-acquisition module acquires the microphone data using LabVIEW™. Fast Fourier transformation (FFT) of time series with 2048 data points and Hanning window with 50% overlap compute acoustic spectra were used in the analysis. The source jet pressure measurement has an uncertainty of 0.1 psi. The microgauge used for linear movements of the nozzle block (for varying the parameter h/d) has an uncertainty of 0.01 mm. A TSI™ Mass Flow Multi-Meter 5300-4 measures the flow rate of acetone-seeded CO_2 with 2% reading accuracy for measurements up to 300 L/min.

B. Design Details of the Coaxial Injector Assembly

Figure 5 shows the design details of the pulsed coaxial injector assembly fabricated with three brass plates. The top plate contains a 3-mm-long, 1.3-mm-diameter cavity through which an underexpanded actuator source jet enters the nozzle block. The second plate has another internal hole that forms the boundary for the resonance phenomenon. A 1 mm (ID) steel tube (with 1.5 mm OD) connects the cavity in the second plate and directs the air jet to flow out from the base

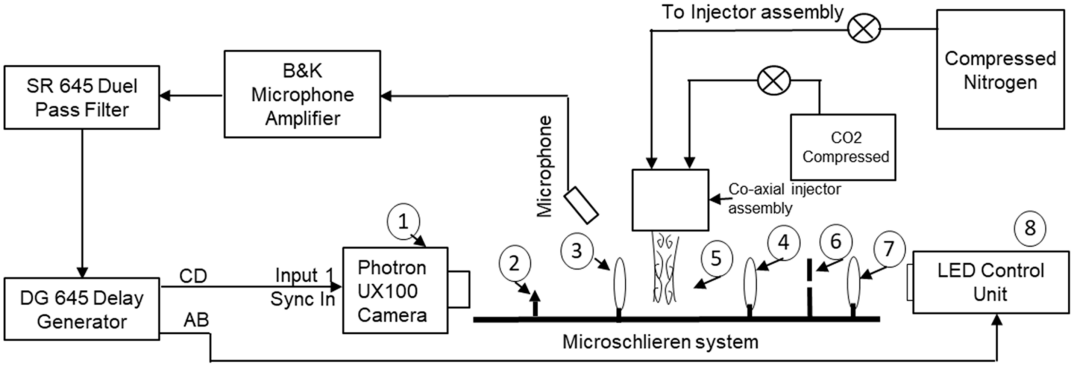

Fig. 2 Experimental setup used for microschlieren imaging used in the present study.

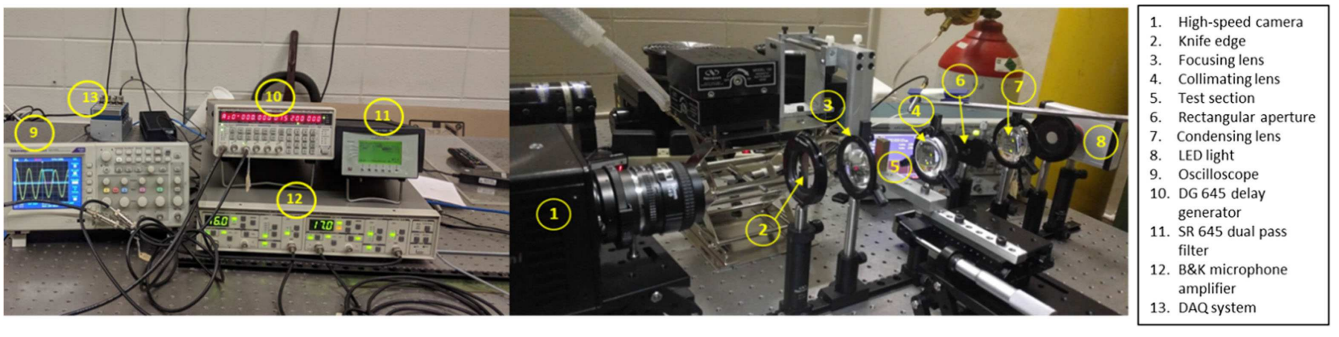

Fig. 3 Microschlieren imaging and DAQ setup used for phased-locked flowfield visualization.

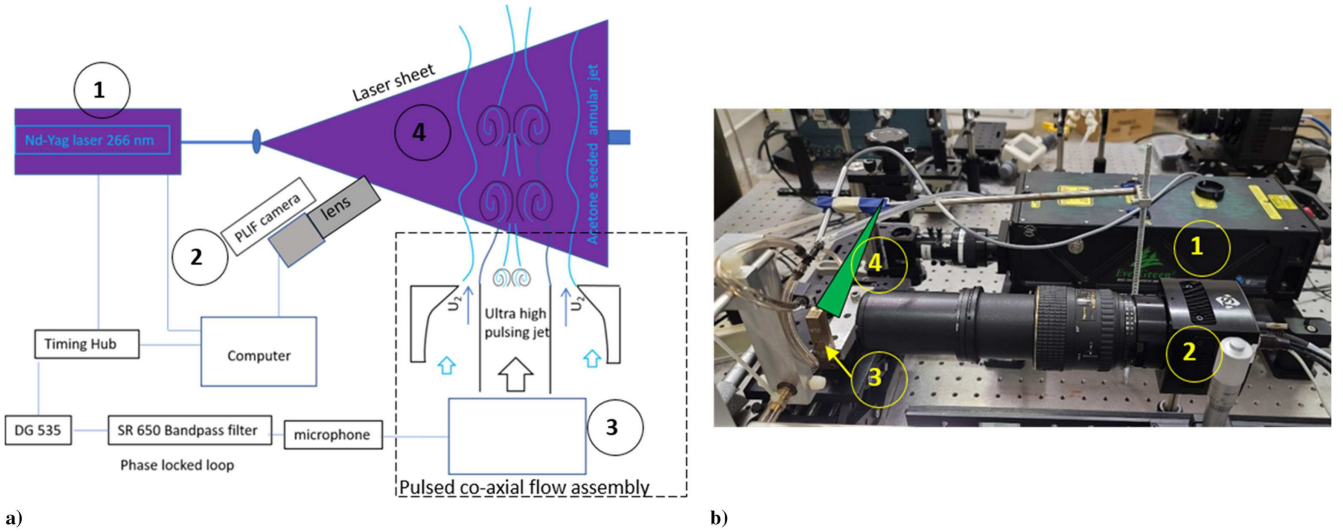

Fig. 4 PLIF measurement system established at Tuskegee University: a) various components of PLIF; b) photograph of PLIF components.

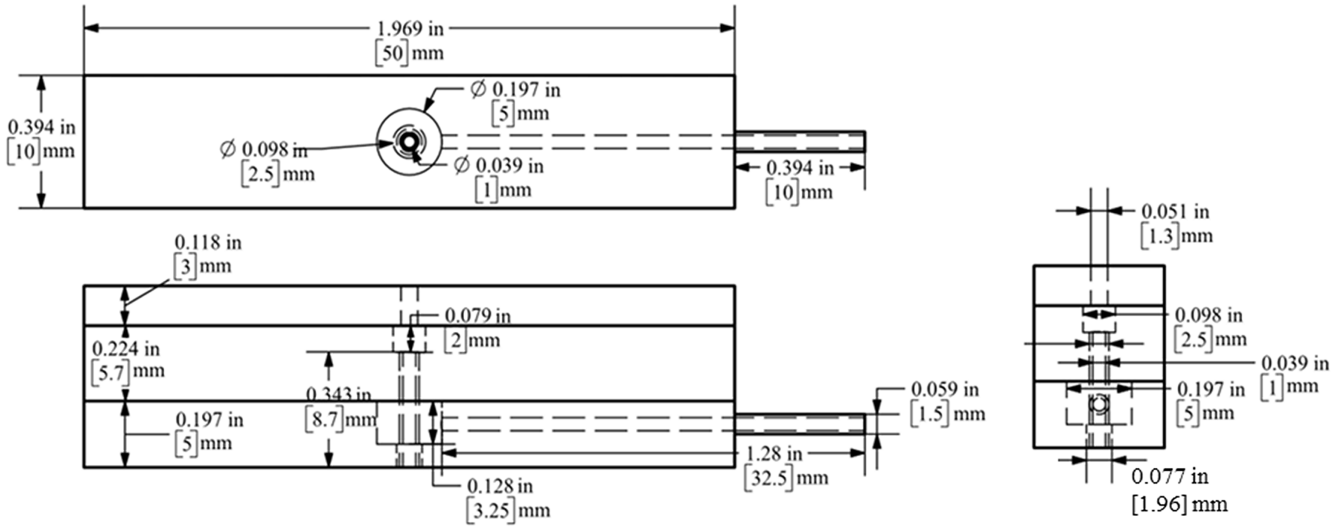

Fig. 5 Design details of the coaxial injector used in this study: a) front and top view; b) side cross-sectional view.

of the third plate. The last plate has a 1.96 mm orifice, so when combined with the second plate and the steel tube with 1.5 mm OD, an annular space is formed outside the 1 mm tube (ID). The internal cavity in plate 3 connects to a steady fluid (CO_2) supply line through a steel tube. The design ensures no interaction or coupling between the coaxial fluids before they reach the exit plane of the assembly.

This assembly has a total internal cavity volume of 20.6 mm^3. An underexpanded source jet supplied from a nozzle of 1.5 mm exit diameter d enters the assembly through a 1.3 mm orifice on the first plate. This source jet produces pulsed flow through the 1-mm-diameter tube integrated into the second and third plates under suitable resonance conditions. This design allows acetone-seeded fluid stream (CO_2) injection through the annular space while the central tube delivers a pulsed actuation jet (N_2). Figure 6a shows a photograph indicating the bottom side of the nozzle assembly, and Fig. 6b shows a zoomed view of the pulsed coaxial nozzle exits. Experiments use two parameters, h/d or nozzle pressure ratio (NPR), where h is the distance of the exit point of the source jet to the actuator cavity, and d is the source nozzle diameter, for frequency control. The present study uses h/d from 1.0 to 1.6 and NPR from 5.8 to 5.5.

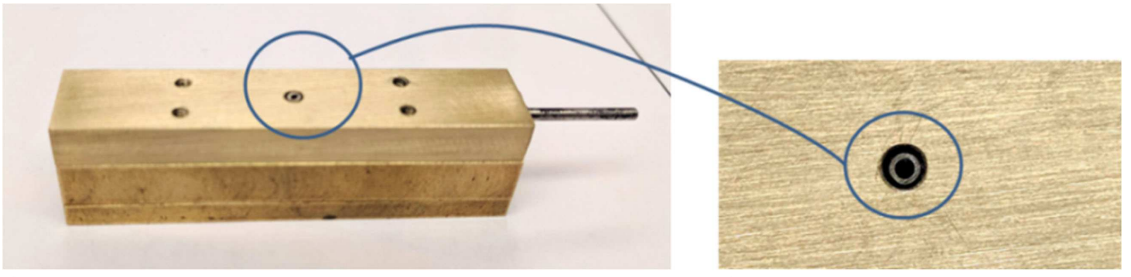

Fig. 6 Photograph of the pulsed coaxial injector indicating a) bottom side and b) zoomed view of the coaxial nozzle exit.

III. Results and Discussion

A. Frequency Characterization of the Pulsed Coaxial Assembly

Figure 7 shows the frequency spectra of the actuator integrated into the nozzle assembly measured using the Grass^{TM} microphone that picks acoustic signals from the nearfield. Figure 1 indicates the microphone's location, 40 mm away from the source jet, oriented at an angle of 45° from the vertical. Acoustic data show that the pulsing frequency varies from 15 to 20 kHz by varying parameter h/d from 1.0 to 1.6, at a constant value of NPR = 5.8. A second microphone (B&K) simultaneously generates real-time signals for phase-locked imaging of the flowfield. A frequency-divided and filtered signal input to the DG645 delay generator outputs digital pulses with appropriate delay (trigger signals) for camera and LED light sources. Section II.A discussed more details of this measurement and the data processing method used for generating the acoustic spectra.

B. Frequency Characterization Using High-Speed Schlieren Images

Apart from microphone measurements, the frequency of the actuator assembly is measured using a high-speed schlieren imaging technique at the University of Tennessee Space Institute (UTSI). Figure 8a shows several temporal schlieren images of the global flowfield captured with a camera operating at 200,000 frames/s. These images indicate the flow structures of the actuation jet and the oscillations of the driving source jet. Note that every time-resolved images treat each pixel as an individual measurement of the fluctuating content present within the flow. Figure 8b shows the results from computing the spectra of each pixel and averaging these spectra across the entire image domain. The dominant peak at approximately 20 kHz is the frequency at which the actuator resonates. The image shown in Fig. 9 maps this high-amplitude peak by considering each pixel independently. Here, the contour levels, representing the normalized intensity of the fluctuating content, appear centered around the 20 kHz peak. These two distinct frequency measurements, one using a microphone and the other using the time-resolved schlieren technique, confirm the ultrasonic frequency excitation capability of the actuator integrated into the coaxial nozzle assembly.

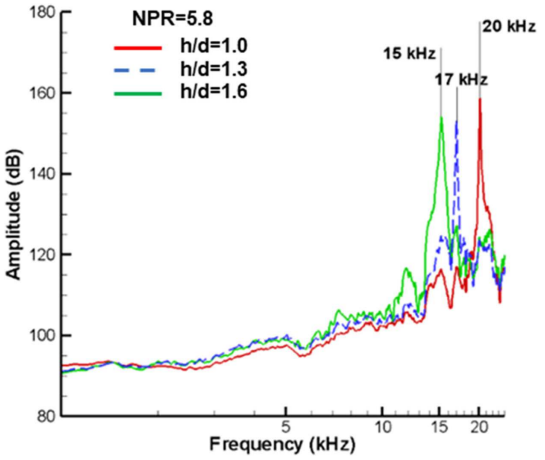

Fig. 7 Frequency spectra of the pulsed coaxial assembly.

C. Phase-Locked Flowfield of the Actuator and Coaxial Jets

Figure 10 shows eight phase-locked, instantaneous images of the actuation jet for a cycle (360°) operating at 15.5 kHz without a coaxial CO_2 stream. Each of these images is 45° phase angle apart and 8 μs time interval. These images capture various phases of the evolution of the pulsed supersonic actuation jet in the coaxial injector assembly. The structures indicate that the flow is supersonic in the first five phases, nearly sonic in the sixth phase, and low subsonic in the last two (270 and 315°). These images indicate that the pulsed actuation generates a high-frequency compressible vortex and a blast wave in the flowfield. The phase-locked images predict a vortex movement of 1.7 mm in 8 μs, which is 1/8th of the period of oscillation of the phenomenon (15.5 kHz) that gives an average velocity of 217 m/s near the exit. The speed slows down to ~125 m/s and then to 88 m/s due to the entrainment and growth of the vortex. Our previous study using a camera with a higher frame rate and reduced resolution also reported that these vortex structures move at ~200 m/s near the exit [16]. The strength of the pulsed jet and vortex front deteriorates in the latter half of the cycle.

Figure 11 shows phase-locked instantaneous images of a coaxial CO_2 stream injected at a pressure of 8 psi while the actuation jet pulses at the same frequency. The characteristics of pulsed actuator flow with the injected stream are very similar to the images as shown in Fig. 10. The exit flow area ratio A_1/A_2 of the present configuration

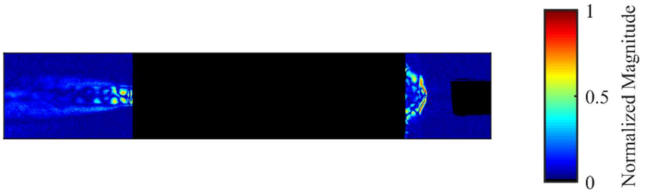

Fig. 9 Contour mapping of the relative intensity of the 20 kHz peak from Schlieren images.

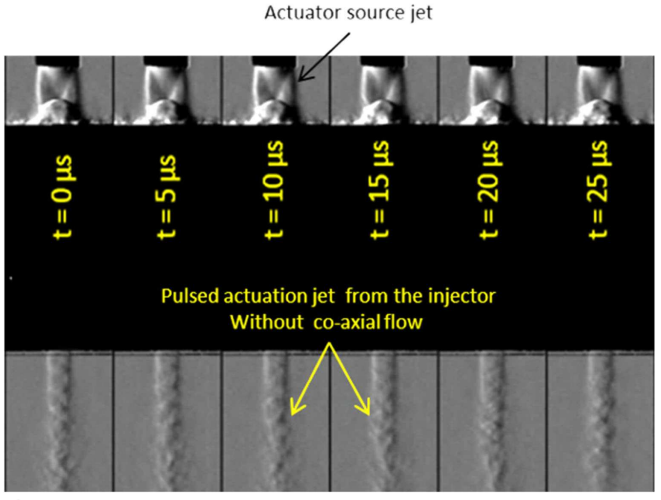

a)

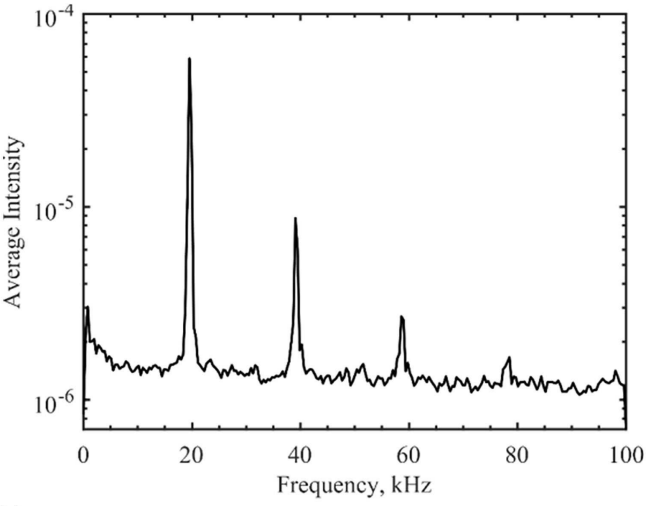

b)

Fig. 8 a) Typical sequence of instantaneous Schlieren images obtained at 200,000 fps. b) Reduction of the time-resolved image sequences to spectral content averaged over the entire imaging domain.

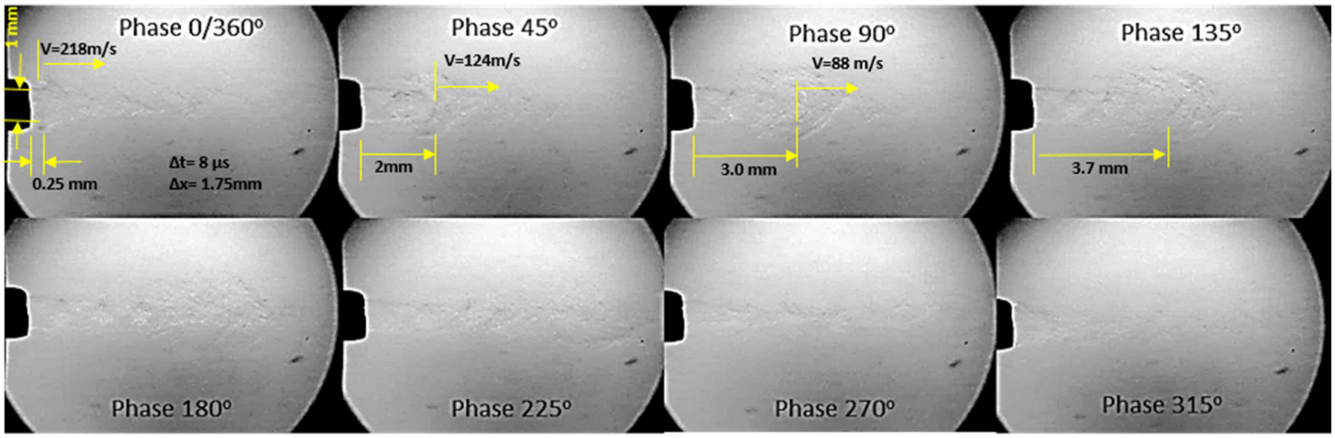

Fig. 10 Phase-locked instantaneous flowfield of central actuation jet without coaxial jet.

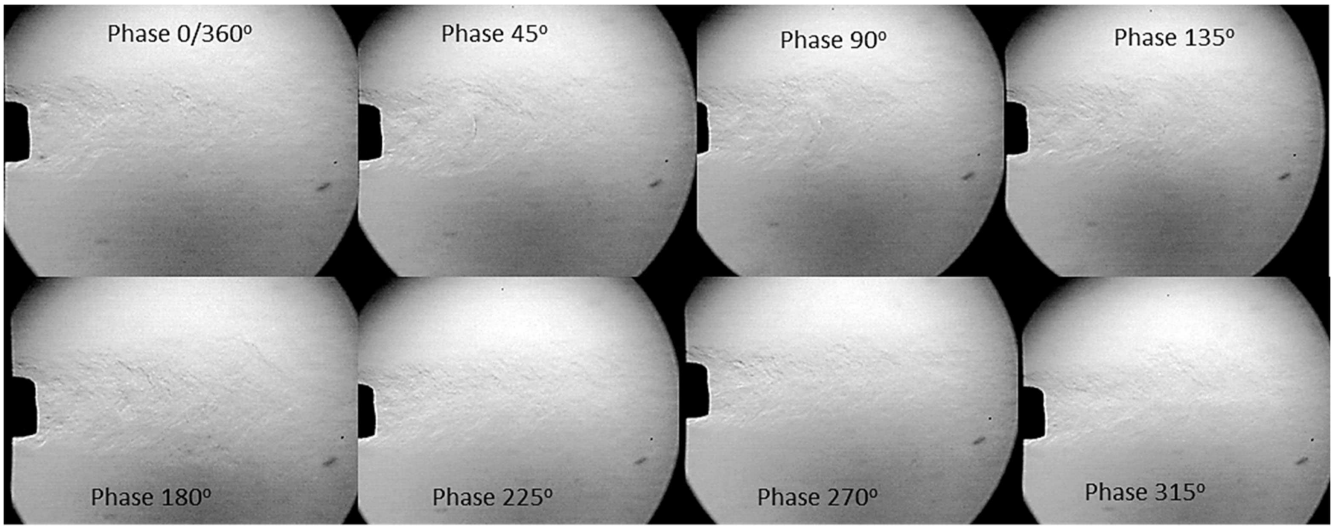

Fig. 11 Phase-locked instantaneous flowfield of the coaxial jet with actuation jet.

is 0.72, where A_1 is the area exit of actuator flow, and A_2 is an area of the annular space. With a pressure ratio of fluids exiting the assembly (P_{act}/P_{stream}) that varies in the range of 1–13 during the pulsed coaxial injection process, the momentum of the actuation jet dominates the flowfield for most of the cycle.

D. Planar Laser-Induced Fluorescence

Figure 12 shows an exit plane configuration of the injector assembly where an annular stream of CO_2 seeded with saturated acetone vapor interacts with the unseeded compressed nitrogen jet. The present experiments use pressure and the flow rate of CO_2 at 8 psi and 4.7 lit/min, respectively. For a given annular exit area of 1.08 mm^2, this flow rate gives an estimated exit velocity of $U_2 \sim 108$ m/s for the seeded CO_2 jet. The exit velocity U_1 of the pulsed jet varies from 10 to 400 m/s during the cycle, giving rise to a velocity ratio $U_1/U_2 = 0.1$–3.7.

Ideally, the saturated vapor exiting the nozzle fluoresces with maximum intensity (red color), and the unseeded actuation jet with zero intensity (black color). Assuming a linear variation between these two extreme values, the intensity of light fluorescence measured at a given location represents the local mixing of acetone with the surrounding unseeded streams. In the present study, we chose

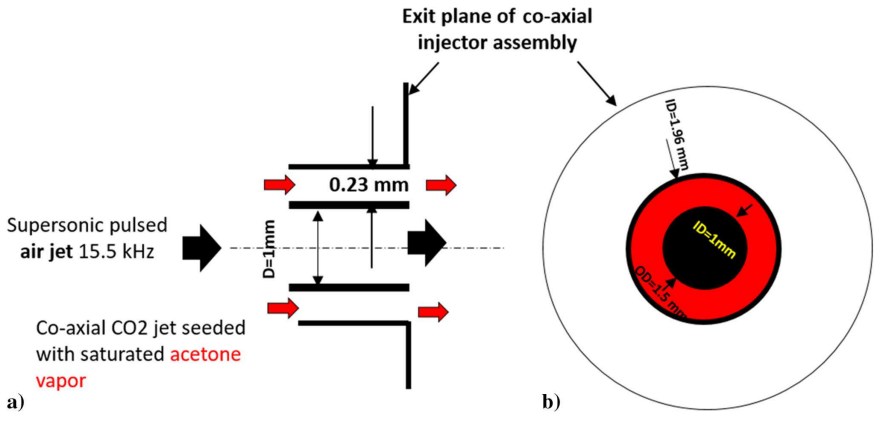

Fig. 12 PLIF configuration for seeded annular jet and unseeded actuation jet.

three configurations for the preliminary experiments: 1) a seed jet alone, 2) a seeded jet with an actuation jet pulsing at 15.5 kHz, and 3) a seeded jet with an actuation jet in a steady mode (without pulsing). Figures 13(i)a–13(i)c show representative instantaneous PLIF images from these three test cases. Figure 13(ii) indicates a magnified flowfield near the exit with more flow features marked. The high-magnification optics and a high-resolution camera (27 MP) capture fine details of these high-speed microscale flows and their mixing characteristics, as indicated in the PLIF images. For all cases, the shear layer boundaries of the seed jet and the natural instabilities present are visible and marked appropriately. For seed jet at 4.7 psi and 5 lit/min, images show the formation of a saturated core up to 10 diameters, and the jet stream seems mixed well with the ambient air further downstream by the natural diffusion mechanism. Figure 13(i)b shows a representative phase of the flowfield when the actuator operates at 15.5 kHz. The pulsing action creates a high-frequency compressible vortex in the same frequency range. This tailored vorticity created at the inner core leads to the entrainment of the seed jet to the actuator flow. The interfacial area of the vortex increases downstream, resulting in increased entrainment, diffusion, and mixing of the seeded CO_2 jet with the actuation jet (N_2) and the ambient air.

The moving shock front created by the pulsed vortex, as indicated in Fig. 13(ii), also improves the mixing of the seeded jet with the actuation jet and the ambient air. The inner shear layer of the seed jet experiences highly unsteady vortex movement and growth downstream. In the third case, the actuation jet operates in steady mode. This case is a classical coaxial flow configuration, as indicated in Fig. 13(i)c. Proper control of parameter h/d adds or eliminates the pulsing action of the actuation jet at the same source jet pressure. In this case, the jet core without seed particles appears to be extended up to $10d$ ($d = 1$ mm, the exit diameter of the actuation nozzle) and then weakens. These images indicate that the compressible shear layer of the steady underexpanded jet offers more resistance to the diffusion of coaxial seed particles into the jet core. The diffusion is favorable when the jet core slows down further downstream. Figure 14 shows the microphone spectra of three cases discussed in Fig. 13. The pulsed coaxial flow shows a distinct frequency at 15.5 kHz. In contrast, the steady coaxial injection shows no specific tones in the spectra besides broadband noise. In steady actuation, the energy is in broadband while it is focused at 15.5 kHz for pulsed actuation. The spectra of the seed jet show low-amplitude broadband noise, indicating natural instabilities in the flow.

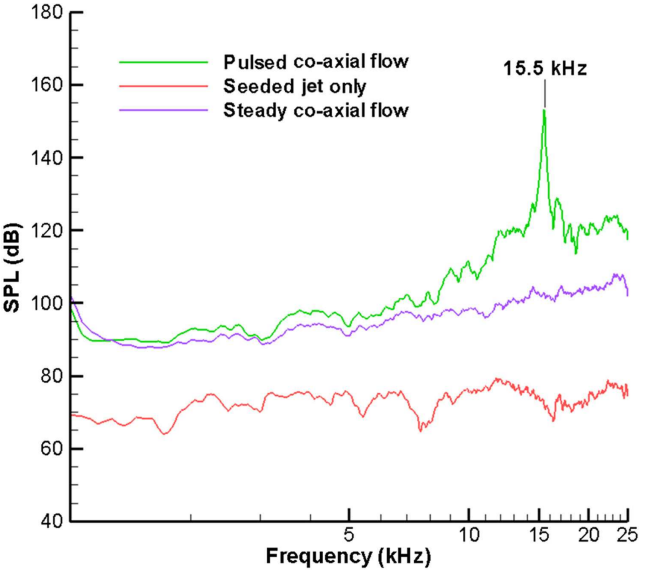

Fig. 14 Spectra measured for three cases shown in Fig. 13i- a) seed jet only, b) pulsed-coaxial flow, and c) steady coaxial flow.

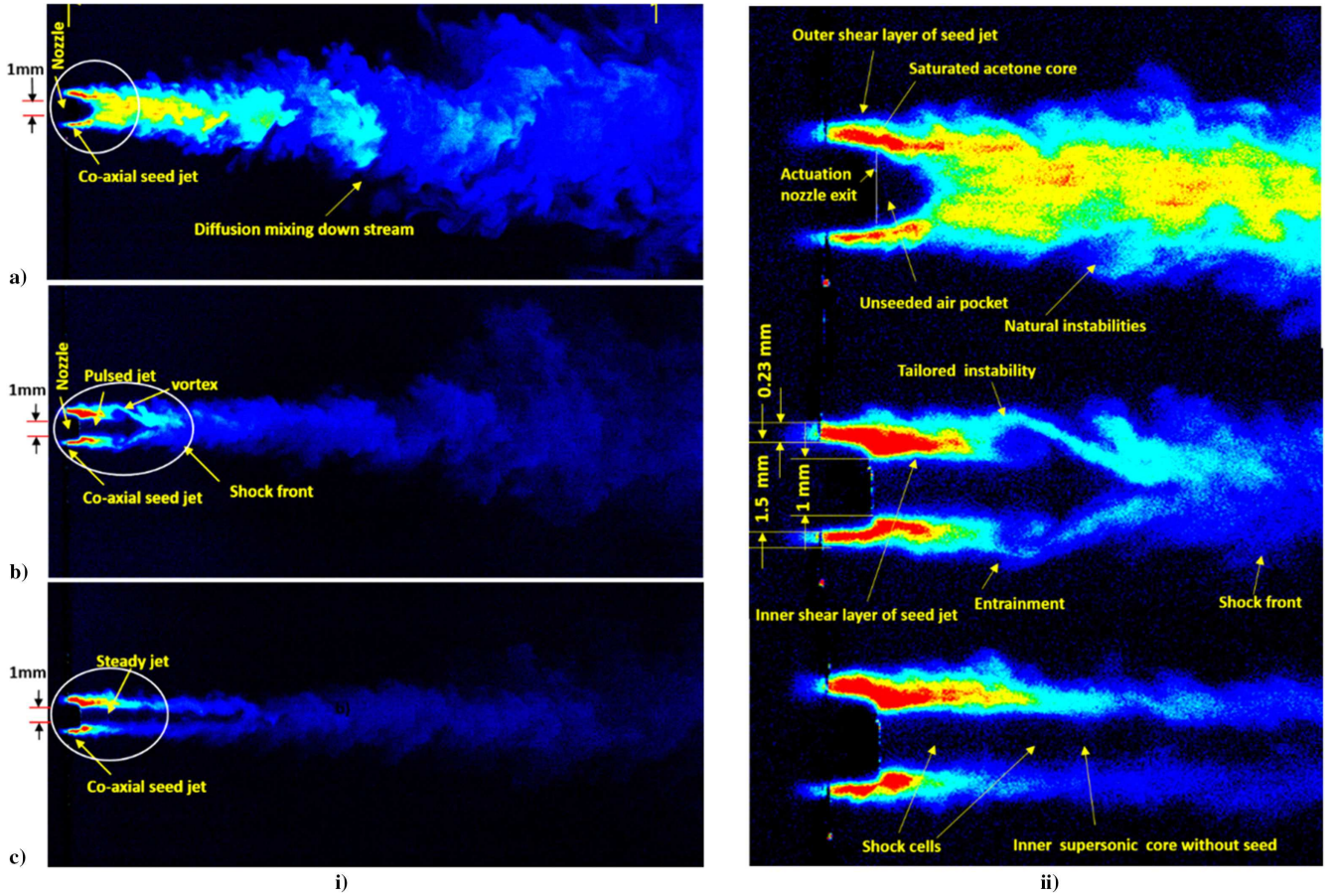

Fig. 13 i) Instantaneous images of a) seed jet alone, b) seeded jet + pulsed actuation jet, and c) seed jet+steady actuation jet; ii) enlarged views at the exit.

Figure 15 shows PLIF images of coaxial flow at various phases, separated by 45°. The flow features are visibly similar to the phase-locked microschlieren images discussed in Fig. 10. These phase images provide helpful insight into the evolution and decay of the central pulsing jet and the overall dynamics of the diffusion process of the seeded annular stream. To directly compare steady and pulsed coaxial injections, Fig. 16 shows eight random images of steady injection, arranged similarly to the phase images displaced in Fig. 15. Qualitatively, it is evident from Figs. 15 and 16 that the flow mixing characteristics are very distinct for steady and pulsed coaxial flow. We noticed earlier that a steady supersonic core tends to be less effective in mixing a coaxial stream and mixing mainly occurs downstream when the core strength deteriorates. Since diffusive mixing is directly related to the relative velocity between the fluid shear layers, the pulsed injection, which provides an opportunity for significant velocity fluctuation in the inner core of the coaxial stream, will be more effective than the steady coaxial injection. Figures 15 and 16 confirm that pulsed coaxial injection is more effective than a regular coaxial injection for mixing under similar flow conditions.

The zoomed view of the flow at the exit, as shown earlier in Fig. 13, reveals the existence of a very small (± 3 μm) asymmetry for the annular exit. The designed thickness of the annular exit is 0.23 mm, and the images show this value on the top and 0.20 mm on the bottom sides. But this asymmetry distorts coaxial flow downstream. To eliminate this asymmetry and to better understand the flow dynamics, three-phase images (45, 180, and 315°) were corrected for symmetry, as shown in Fig. 17. For this purpose, the upper half of the image is reflected along the axis of symmetry.

Figure 17 also displays a microschlieren image of the actuation jet at the same phase angle. These images show three key characteristics, an evolving vortex, a moving shock wave, and a wavefront, which significantly impact the mixing process involved with the pulsed coaxial injection. In general, we can identify four different mixing mechanisms from these images: 1) vortex-induced mixing, 2) shock-induced mixing, 3) mixing due to growth and entrainment of vortex downstream, and 4) natural diffusion from the outer shear layer of the seeded stream. In the first mechanism, the compressible vortex formed near the nozzle exit entrains the surrounding seeded stream saturated at the nozzle exit and moving forward with a velocity of 200+ m/s. The actuation jet velocity is sonic at the nozzle exit, and it evolves as an underexpanded jet core downstream surrounded by the coaxial seeded stream. The diffusion of the seeded stream to the compressible shear layer of the jet core is minimum near the nozzle exit.

In the second shockwave-induced mixing mechanism, the pulsing action produces a shock wave, as indicated in Fig. 17a, that moves faster than the jet front, causing breakdown of the seeded coaxial fluid shear layer ahead of it. This action creates fragmented structures with a high concentration of seed particles surrounded by the unseeded actuation jet. The moving shock drags some of these fragmented structures and their forward motion, creating a plume of disintegrated seed jet surrounded by a coaxial stream, as evident from Fig. 17b, causing better mixing with ambient air. The third mixing mechanism owes to the growth and entrainment of the vortices in the streamwise direction. In the present image data, the PLIF camera setup provides a field of view up to 30 mm in the streamwise direction and 20 mm in the spanwise direction. The images in Figs. 17a and 17b are temporally connected. For a phase angle difference of 135° (from 45 to 180°), the vortex and the wavefront move a period of 24 μs. Since the cycle period is 64 μs as measured by the spectra (15.5 kHz), the second vortex eye in Fig. 17a must be 40 μs separated from the wavefront seen for phase angle 180°. This vortex 2 captured in the image is the one that precedes vortex 1. Locations of vortices 1 and 2 are separated by a distance of 10 mm, as indicated in a scale shown in Fig. 17a. We can estimate an average velocity of 156 m/s for its movement for a cycle from the nozzle exit. This estimate is close to the average velocity observations from phased microschlieren images shown in Fig. 10.

Figure 17a marks two more vortex eyes in the image as vortex 3 and vortex 4, which must be preceded by vortex 2 in order. The velocity estimate shows that growth and entrainment slow down to ~65 and 60 m/s, respectively, for these two vortices.

Finally, the fourth mixing mechanism is the natural diffusion to the ambiance from the outer and inner shear layers of the moving vortices and the coaxial streams. Apart from the tailored vortices numbered 1–4, the natural instability-driven vortex patterns are visible when

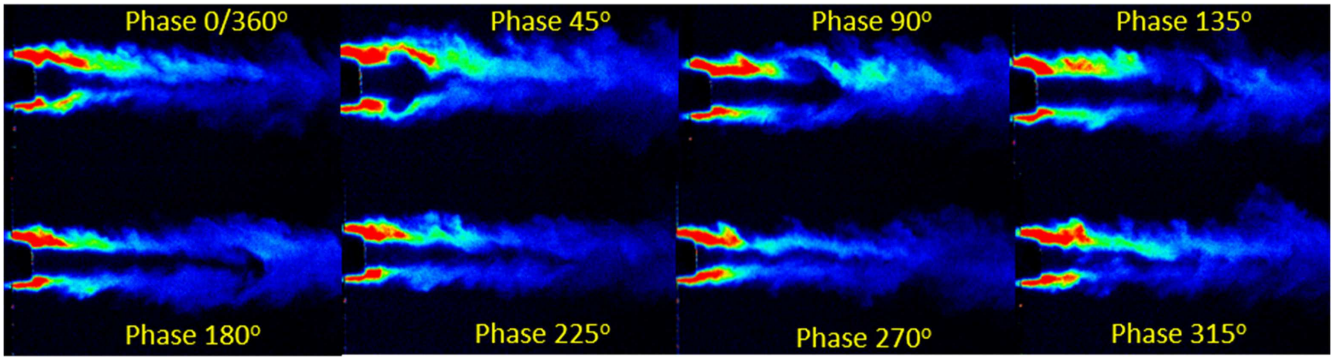

Fig. 15 Eight instantaneous phases of acetone-seeded CO_2 jet with actuation jet pulsing at 15.5 kHz.

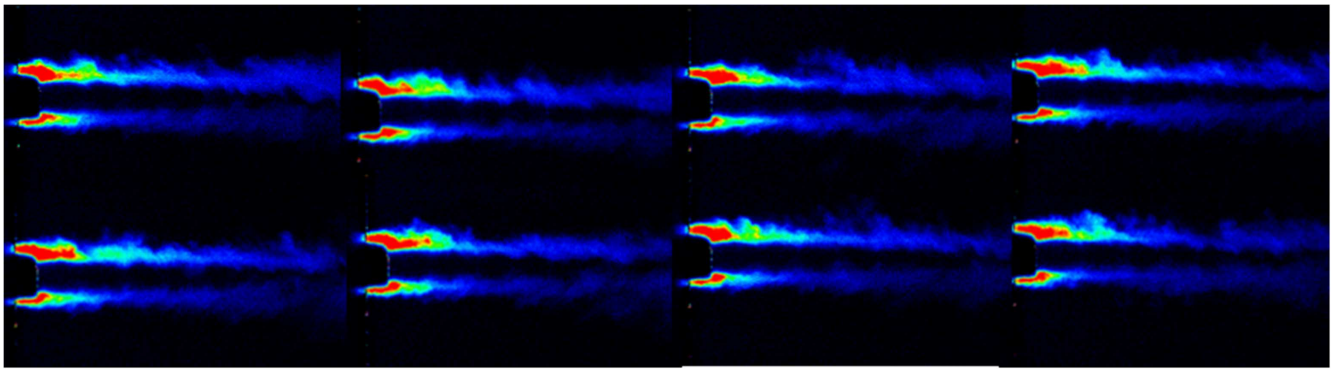

Fig. 16 Eight random instantaneous images of seeded jet with steady jet actuation jet at the core.

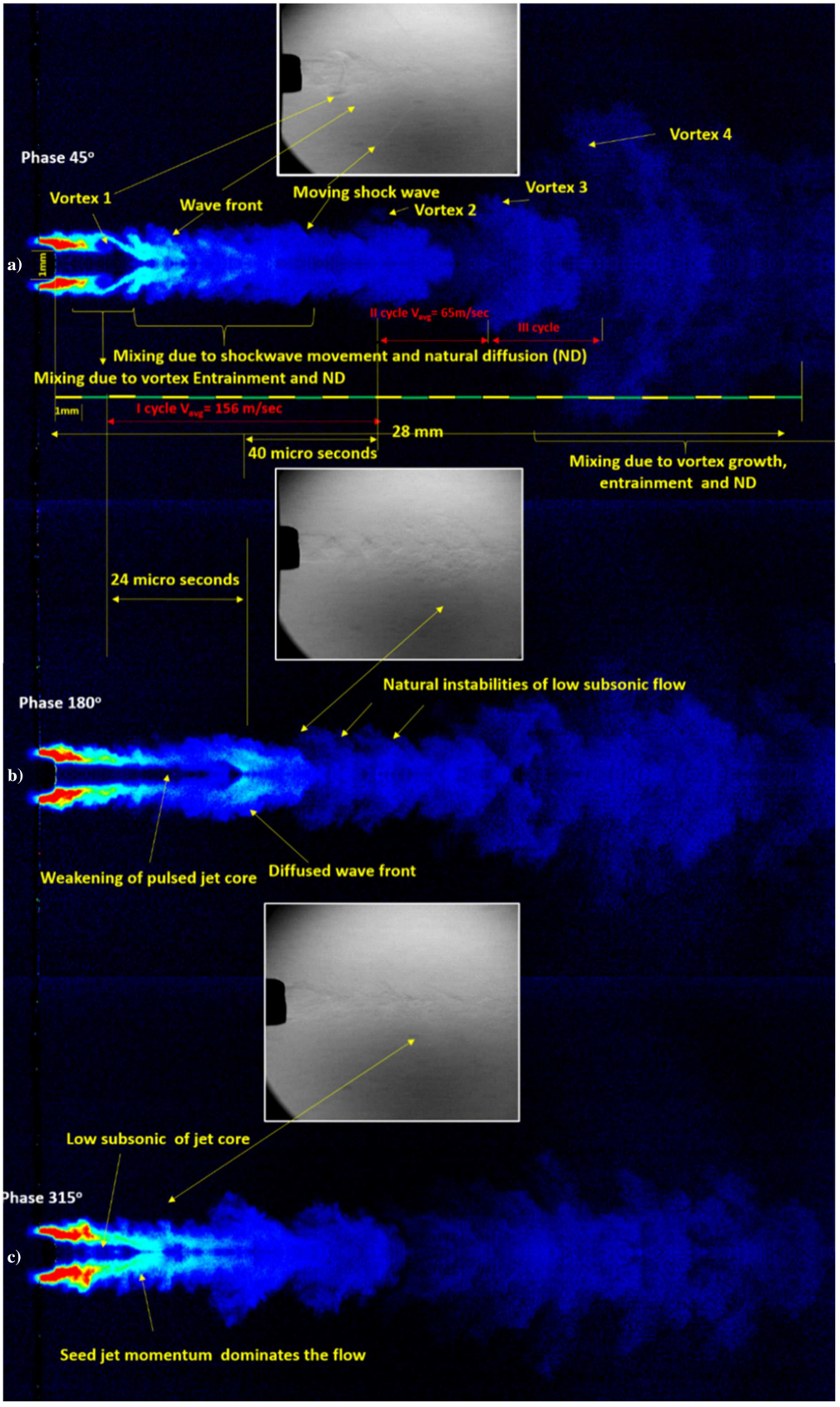

Fig. 17 Symmetry correction for the flow dynamics analysis of three phases of the coaxial pulsed flowfield.

the actuation stream slows to subsonic speeds. Figure 17b shows a weakening of the actuation core and the formation of such natural vortices in the flow along with the diffused wavefront vortex 1. In the final phases, the actuation jet momentum drops considerably, so the seeded jet momentum dominates the flow and structures. Figure 17c shows that, at the actuation jet's light subsonic speed, the seed jet core converges to the center, and the mixing occurs mainly due to the natural diffusion process.

Figure 18 shows averaged images for each case calculated using 250 instantaneous PLIF images. Since each instantaneous image

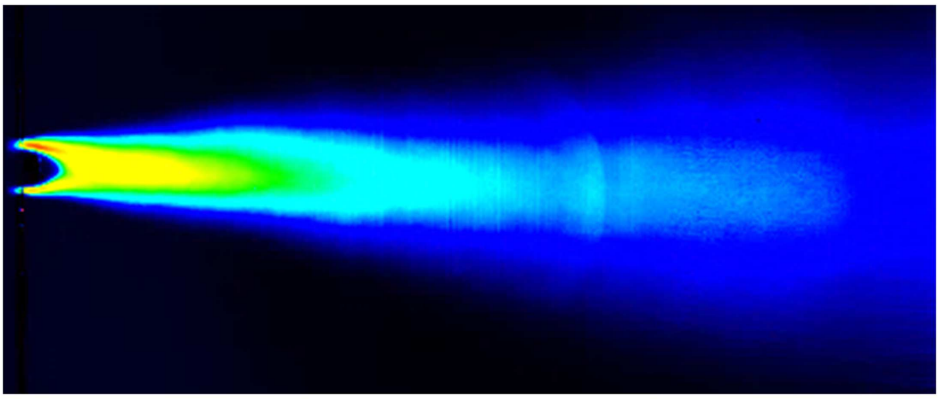

a) Seed jet-the average intensity of pixels in the entire image – 44.3

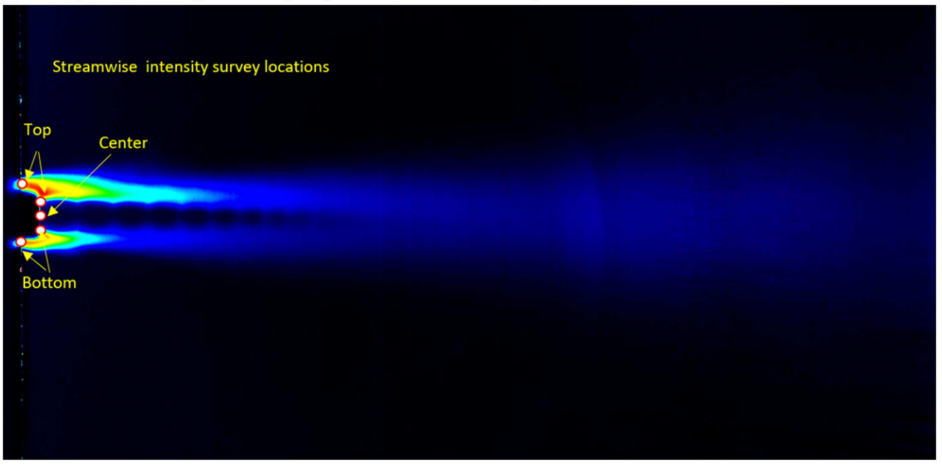

b) Seed jet +steady jet-The average intensity of pixels in the entire image – 7.5

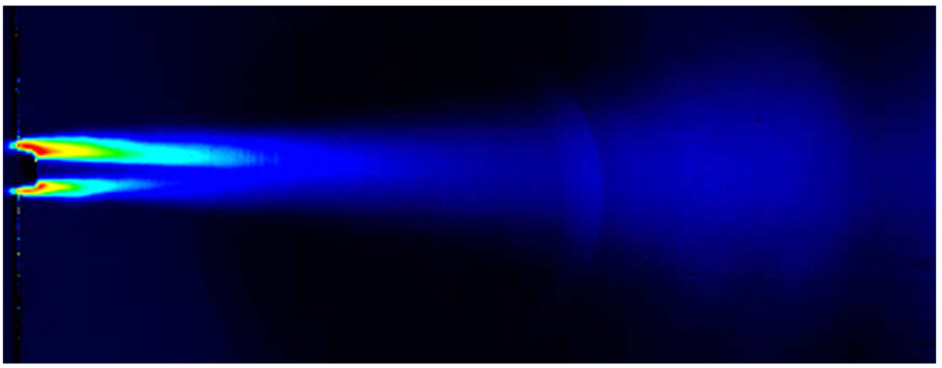

c) Seed jet + pulsed jet- The average intensity of pixels,=15.9 of the entire image, ~114% more than case b)

Fig. 18 Average of 250 instantaneous PLIF images: a) seed jet alone; b) seed jet and steady actuation; c) seed jet and pulsed actuation at 15.5 kHz.

contains information on 4–5 cycles, as discussed in Fig. 17, the average image represents information on ∼1000 cycles for the pulsed injection case. These averaged images provide a comprehensive view of all three cases' mixing characteristics and provide reasonably accurate quantitative estimates of mixing effectiveness between the two cases, steady versus pulsed actuation. The intensity of each pixel in the averaged PLIF image is proportional to the average acetone concentration around that elemental volume for the image sequences selected. An average of all pixel intensity provides a simple estimate of acetone concentration in a given field of view for a particular case. For the first case, seed jet alone, this number is 44.3. For the second case, when an unseeded steady actuation jet flows through the core, the acetone content we measure as average intensity in the same field of view changes due to fast relative motion. The average intensity of pixels measured for this case is 7.5. The same calculation for pulsed injections shows this average intensity value as 15.9. This calculation estimates that the mixing effectiveness of pulsed coaxial injection is 114% more than the steady coaxial injection, as indicated in Fig. 19 for the same injection pressure.

Figures 19a–19h show the average intensity profiles of pixels at various streamwise locations of images shown in Fig. 18. The acetone seed jet profiles (green curve) show two maxima up to $x/d = 2$ and then diffuse into a single jet structure. Seed density remains high in the core region and drops in the streamwise direction as expected, and the jet width increases gradually as the jet diffuses in the downstream direction. The unseeded steady and pulsed coaxial flow (blue and red curves) profiles show two distinct peaks in all streamwise locations. A slight geometric asymmetry at the exit nozzles creates more seeded acetone jet flow at the top than at the bottom. Since pixel intensity directly correlates to the seed density, this results in an asymmetric intensity profile with higher intensity on the top location of the assembly indicated in Fig. 18.

The intensity profiles in all x/d locations indicate that the pulsed coaxial flow creates a significantly improved distribution of seeded acetone in the field of view than the steady jet operates at the same

pressure. Profiles e–h (Fig. 19) indicate the mixing of the seeded jet, and the unseeded actuation jet increases as it flows downstream. As discussed in Fig. 17, this enhanced mixing is attributed to the entrainment and growth of high-frequency vortex generated by the pulsed jets and through the shock wave diffusion through the interface of the seeded and unseeded flow downstream. Comparison of the jet width of steady and pulsed coaxial also gives indications of better mixing between the seeded jet and unseeded supersonic actuation jet when pulsing at 15.5 kHz. The profiles examined at various locations of x/d also reflect the mixing effectiveness of pulsed actuation estimated based on the average image intensity.

To better understand the mixing characteristics, we choose five locations on the exit of the injector assembly, as indicated in Fig. 18b, the top, bottom, center, and top and bottom shear locations to plot the intensity profile along the streamwise direction. Figure 20 represents the normalized intensity of the averaged image of the seed jet at these five locations. These profiles show that intensity varies continuously in the axial direction. A careful look at the profiles of the seed jet indicates that the intensity at the top location is high compared to the bottom side due to the asymmetry at the exit. A slight downward inclination of the seeded jet core, as evident from Fig. 18a, results in higher intensity values at the bottom location on the downstream side, as observed in Figs. 20a and 20b. Figures 21 and 22 show the intensity profiles of pulsed coaxial jets and steady coaxial jets at various exit locations. These profiles show the same level of intensity level near the nozzle exit.

Figures 21a and 22a (green curve) indicate the centerline intensity in the axial direction for the pulsed and steady coaxial flow configurations. The mixing is minimum near the nozzle exit for steady coaxial flow. As evident from Fig. 21b, the pulsed flow provides significantly enhanced mixing near the nozzle exit for the same pressure input to the actuation source jet. Far downstream, the centerline intensity levels become similar in both configurations. A comparison of acetone intensity in the shear layer profile shown in Figs. 21b and 22b indicates that the pulsed coaxial actuation provides enhanced mixing characteristics in the shear layer than steady coaxial injection. The sawtooth intensity patterns in Fig. 22b are due to the steady jet's underexpanded jet structure at 65 psi pressure. The compressible shear layer of the jet at this high pressure offers more resistance to diffusion across the shear layer at supersonic speed. Profiles in Fig. 22a also indicate that the higher injection pressure does not favor mixing near the injector.

PLIF data show that pulsed jets operating at 15.5 kHz improve ~114% more mixing than a steady underexpanded jet operating in the same pressure input pressure. The experiments were conducted with an actuator operating at 11–20 kHz to understand this phenomenon further. Figure 23 shows spectra for pulsed steady coaxial flow and the seed jet configuration. Another actuation case explored is actuator resonance in a broadband regime where fluid oscillation and periodic phenomenon appear in the actuator assembly. This broadband spectrum is shown in Fig. 23b with a black curve. The effect of this actuation on the average PLIF pixel intensity of 250 images is summarized in Fig. 24. The average pixel intensities of various configurations are 44.3, 7.4, 9.8, 11.2, 15.9, 13.1, and 11.9, respectively for seed jet, and various actuation cases-steady, broadband, 11 kHz, 15.5 kHz, 18 kHz, and 20 kHz. The percentage change from steady jet mixing value (7.4) to that of various active actuation cases - broadband, 11 kHz, 15.5 kHz, 18 kHz, and 20 kHz - are 33, 50, 114, 76, and 60%, respectively. The highest amplitude actuation with 15.5 kHz provides the maximum value for the average intensity.

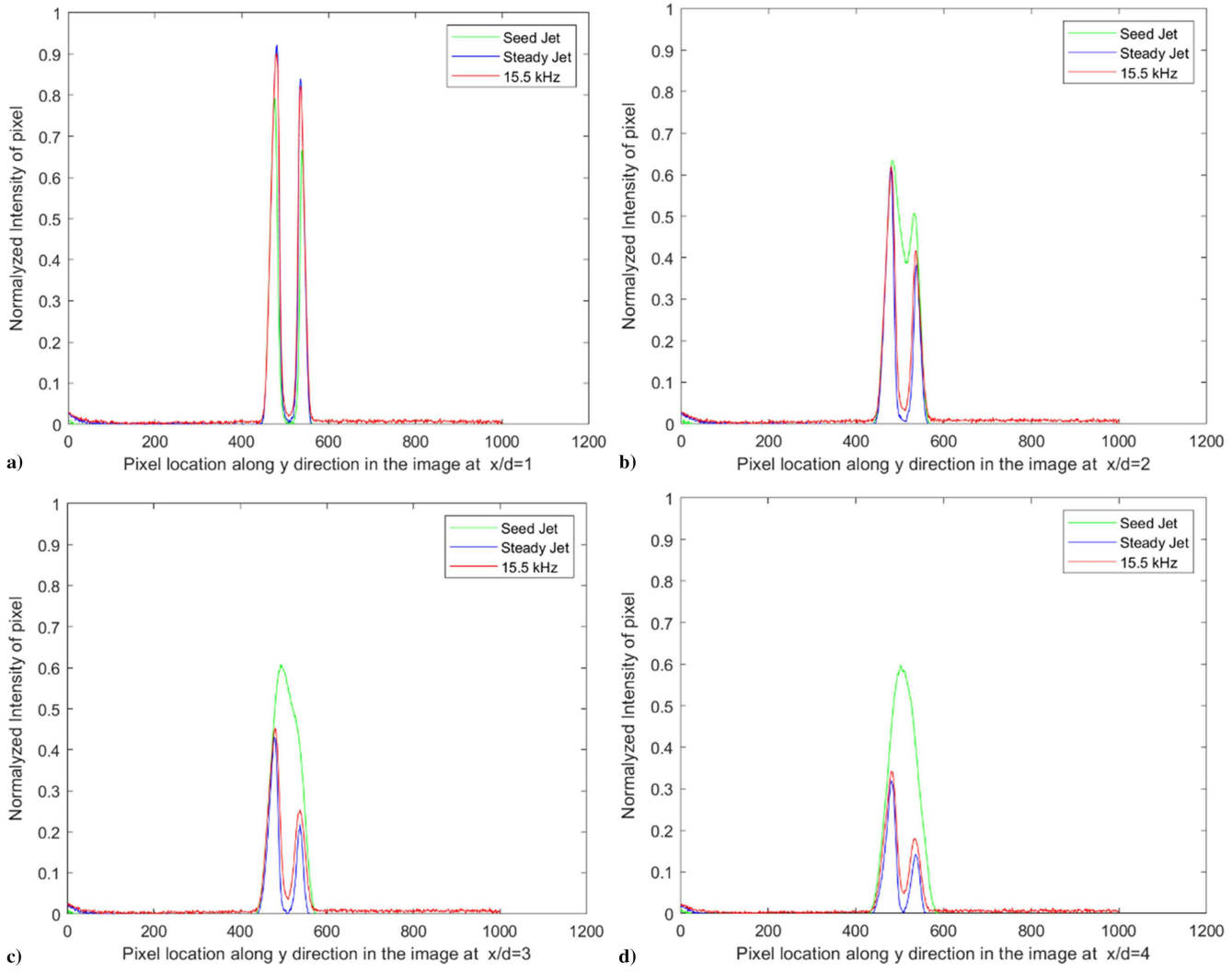

Fig. 19 Normalized intensity profiles of averaged images shown in Fig. 18 at various x/d locations.

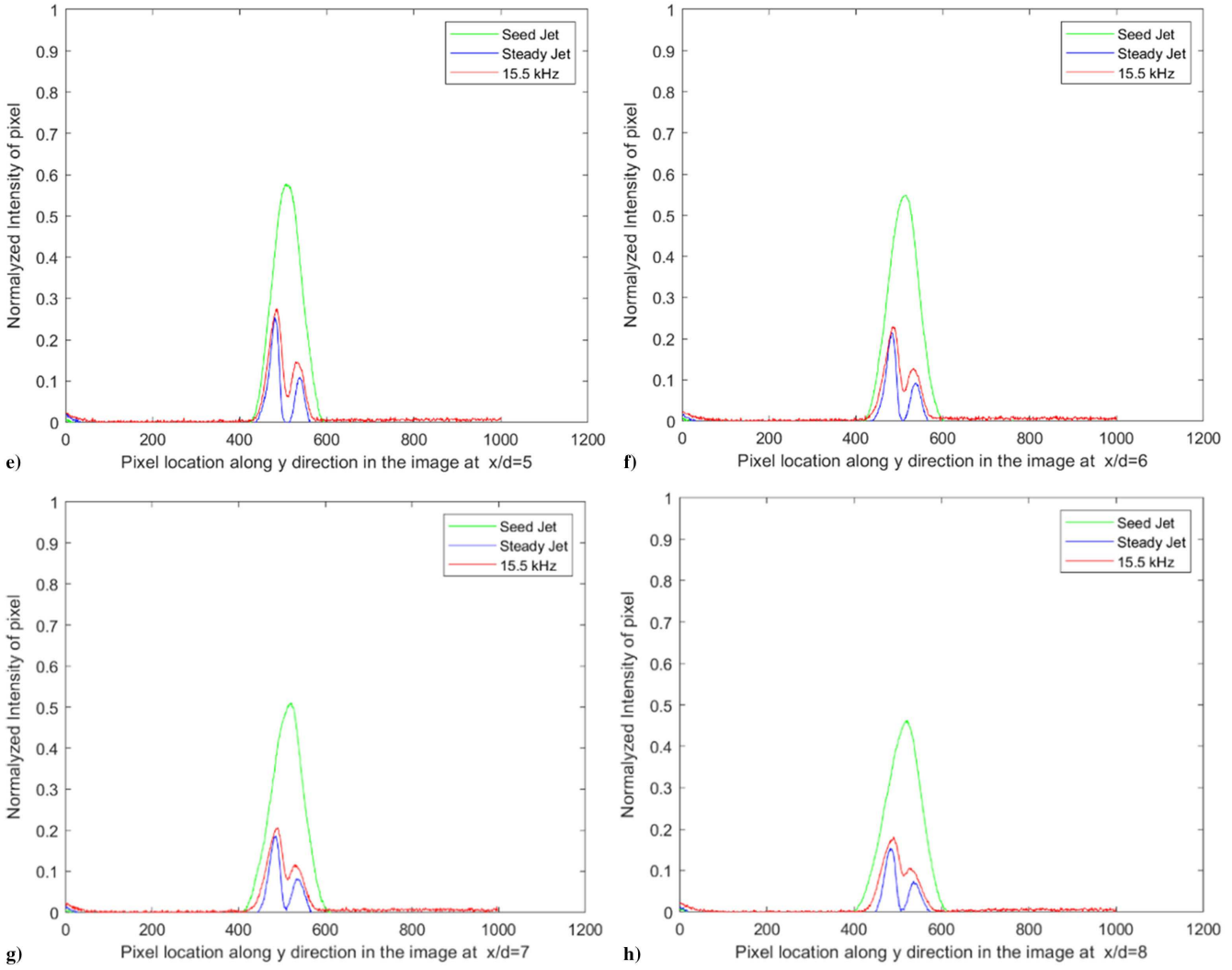

Fig. 19 (Continued)

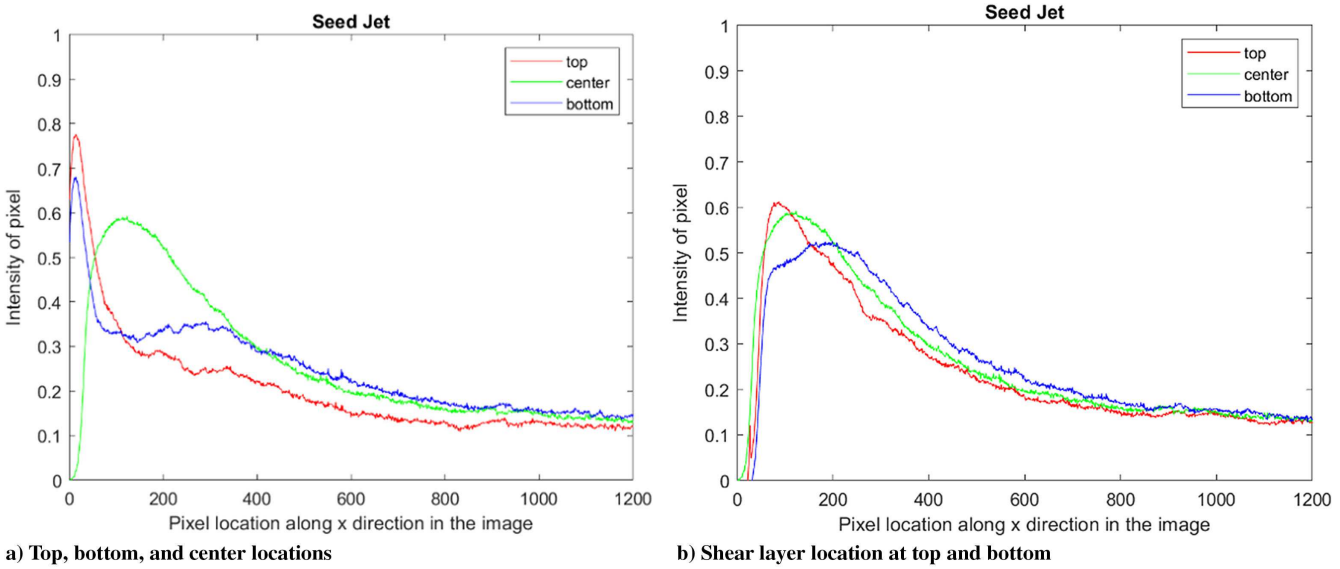

a) Top, bottom, and center locations **b) Shear layer location at top and bottom**

Fig. 20 Normalized intensity profiles of averaged images of seed jet in streamwise direction at various locations.

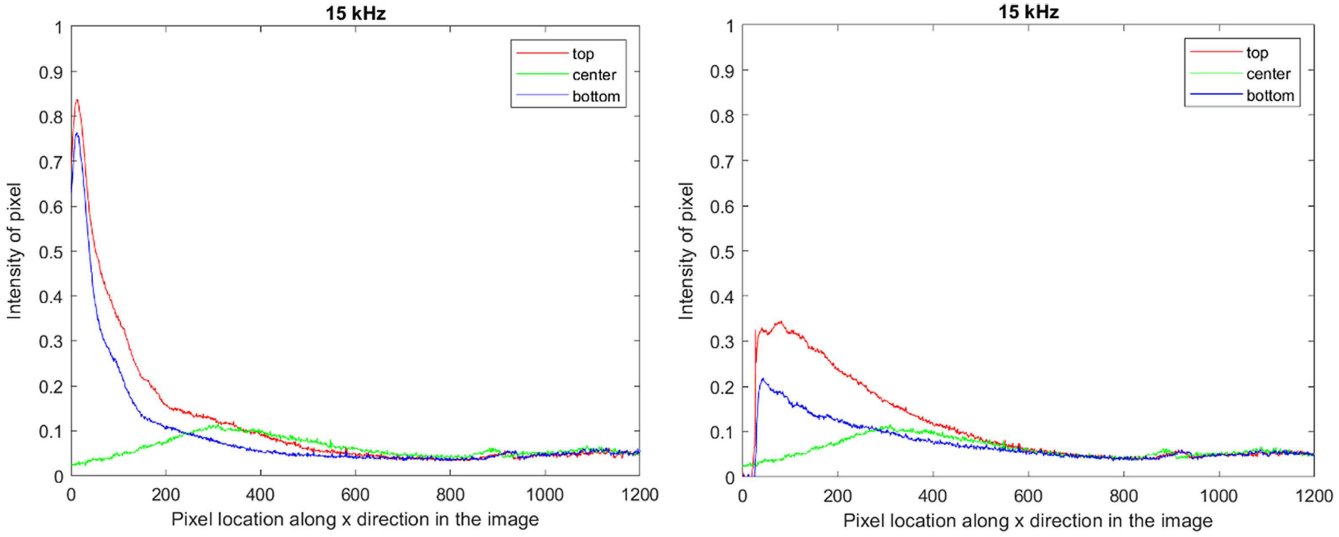

a) Top, bottom, and center locations b) Shear layer locations at the top and bottom

Fig. 21 Normalized intensity profiles of averaged images of pulsed jet in streamwise direction at various locations.

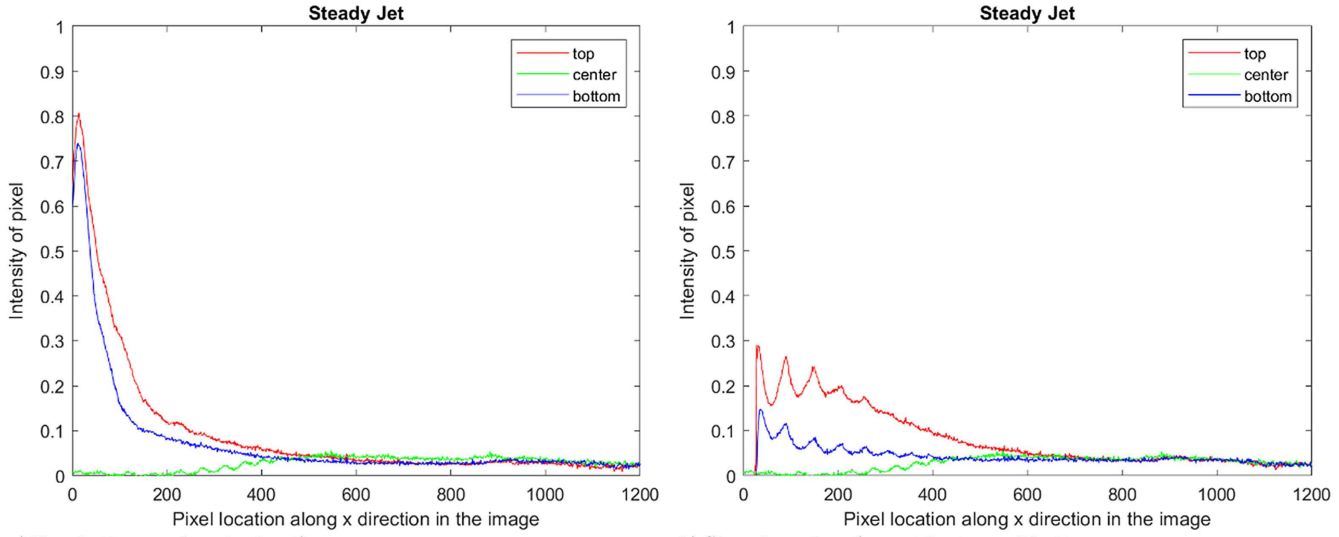

a) Top, bottom, and center locations b) Shear layer locations at the top and bottom

Fig. 22 Normalized intensity profiles of averaged images of steady jet in streamwise direction at various locations.

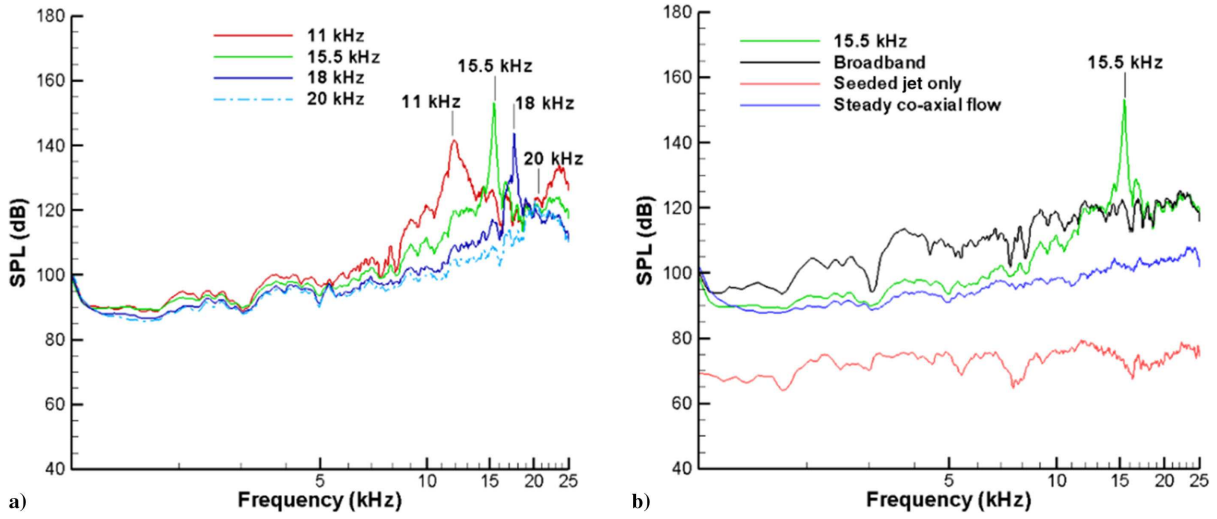

a) b)

Fig. 23 Spectrum of coaxial jets used for this study: a) frequency sweep of pulsed jet; b) spectra of steady, broadband, and seed jet.

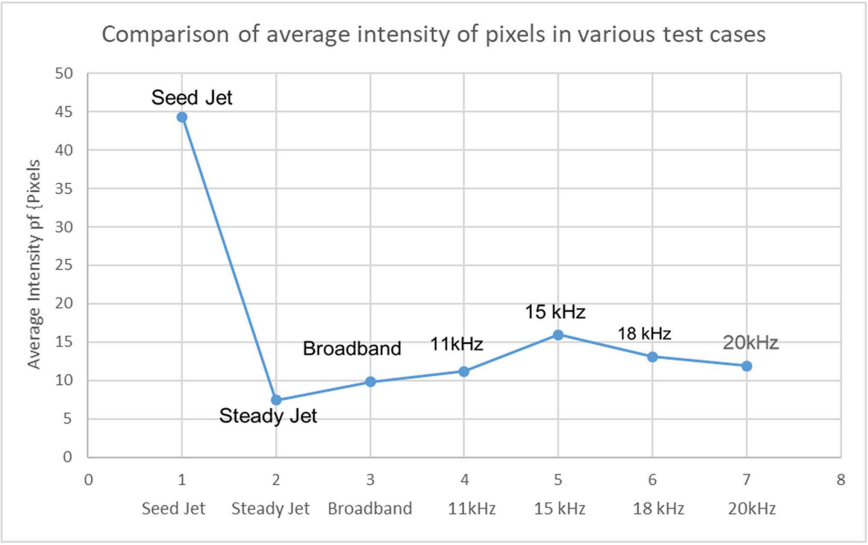

Fig. 24 Summary of the average intensity of acetone-seeded stream calculated from averaged images for various test cases.

IV. Conclusions

This paper reports an experimental study on an active, pulsed coaxial jet injection assembly integrated with ultrahigh-frequency pulsed microactuators. The assembly steadily injects a fluid through an annular space around a 1 mm nozzle through which a supersonic actuation air jet flows out at a frequency range of 11–20 kHz. The pulsed air jet develops a high-frequency compressible air vortex in the injected flowfield and entrainment of the jet injected through the annular space, causing significantly improved mixing between the two fast-moving fluids. The pulsed coaxial flowfield is analyzed using phase-locked microschlieren imaging and the PLIF technique. PLIF uses saturated acetone introduced to the annular jet for quantitative mixing measurements. The experimental data show that pulsed injection enhances mixing due to vortex entrainment, shock blasting through the fluid stream, vortex growth, and natural diffusion through the outer shear layers of the flow compared to a configuration with steady actuation. The estimate shows that the compressible pulsed vortex generated by the actuation jet has an initial speed of 216 m/s and an average speed of 156 m/s in its first cycle close to the exit. The vortex velocity drops 65 m/s after 64 μs. PLIF image analysis estimates that pulsed injection significantly improved mixing by 50–115% compared to steady coaxial injection under the same injection pressure conditions. The data indicate that the actuation jet's unsteadiness amplitude and frequency strongly influence the high-speed mixing phenomenon. Particle image velocimetry experiments and parametric variations to these configurations are ongoing and will be reported in the future.

Acknowledgment

National Science Foundation supports this work through Grant 1900177.

References

[1] Ritchie, B., Mujumdar, D., and Seitzman, J., "Mixing in Co-Axial Jets Using Synthetic Jet Actuators," *38th Aerospace Sciences Meeting and Exhibit*, AIAA Paper 2000-0404, 2000.

[2] Davis, S. A., and Glezer, A., "Mixing Control of Fuel Jets Using Synthetic Jet Technology: Velocity Field Measurements," *37th Aerospace Sciences Meeting and Exhibit*, AIAA Paper 1999-0447, 1999.

[3] Broadwell, J. E., and Mungal, M. G., "Large Scale Structures and Molecular Mixing," *Physics Fluids*, Vol. 3, No. 5, 1991, pp. 1193–1206.

[4] Kraus, D. K., and Cutler, A. D., "Mixing of Swirling Jets in a Supersonic Duct Flow," *Journal of Propulsion and Power*, Vol. 12, No. 1, 1995, pp. 170–177.
https://doi.org/10.2514/3.24007

[5] Cutler, A. D., and Doerner, S. E., "Effects of Swirl and Skew Upon Supersonic Wall Jet in Crossflow," *Journal of Propulsion and Power*, Vol. 17, No. 6, 2001, pp. 1327–1332.
https://doi.org/10.2514/2.5882

[6] Drozda, T. G., Baurle, R. A., and Drummond, J. P., "Impact of Flight Enthalpy, Fuel Stimulant, and Chemical Reactions on the Mixing Characteristics of Several Injectors at Hypervelocity Flow Conditions," NASA Langley Research Center, May 2016, https://ntrs.nasa.gov/archive/nasa/casi.ntrs.nasa.gov/20160009131.pdf [retrieved May 2017].

[7] Gruber, M. R., Nejad, A. S., Chen, T. H., and Dutton, J. C., "Transverse Injection from Circular and Elliptic Nozzles into a Supersonic Crossflow," *Journal of Propulsion and Power*, Vol. 16, No. 3, 2000, pp. 449–457.
https://doi.org/10.2514/2.5609

[8] VanLerberghe, W. M., Santiago, J. G., Dutton, J. C., and Lucht, R. P., "Mixing of a Sonic Transverse Jet Injected into a Supersonic Flow," *AIAA Journal*, Vol. 38, No. 3, 2000, pp. 470–479.
https://doi.org/10.2514/2.984

[9] Shigeru, A., ArifNur, H., Shingo, M., Kei, I., and Yasuhiro, T., "Fundamental Study of Supersonic Combustion in Pure Air Flow with Use of Shock Tunnel," *Acta Astronautica*, Vol. 57, Nos. 2–8, 2005, pp. 384–389.
https://doi.org/10.1016/j.actaastro.2005.03.055

[10] Menon, S., "Shock Wave Induced Mixing Enhancement in Scramjet Combustors," *27th Aerospace Sciences Meeting*, AIAA Paper 1989-0104, 1989.
https://doi.org/10.2514/6.1989-104

[11] Ben-Yakar, B., Mungal, M. G., and Hanson, R. K., "Time Evolution and Mixing Characteristics of Hydrogen and Ethylene Supersonic Crossflow," *Physics of Fluids*, Vol. 18, No. 2, 2006, Paper 026101.
https://doi.org/10.1063/1.2139684

[12] Hsu, K., Carter, C. D., Gruber, M. R., and Tam, C., "Mixing Study of Strut Injectors in Supersonic Flows," *AIAA Joint Propulsion Conference*, AIAA Paper 2009-5226, 2009.
https://doi.org/10.2514/6.2009-5226

[13] Hongbin, G., Zhi, L., Fei, L., Lihong, C., Shenglong, G., and Xinyu, C., "Characteristics of Supersonic Combustion with Hartmann-Sprenger Tube Aided Fuel Injection," *AIAA Conference*, AIAA Paper 2011-2326, 2011.
https://doi.org/10.2514/6.2011-2326

[14] Solomon, J. T., Foster, C., and Alvi, F. S., "Design, and Characterization of High-Bandwidth, Resonance Enhanced, Pulsed Microactuators: A Parametric Study," *AIAA Journal*, Vol. 51, No. 2, 2013, pp. 386–396.
https://doi.org/10.2514/1.J051806

[15] Uzun, A., Solomon, J. T., Foster, C. H., Oates, W. S., Hussaini, M. Y., and Alvi, F. S., "Flow Physics of a Pulsed Microjet Actuator for High-Speed Flow Control," *AIAA Journal*, Vol. 51, No. 12, 2013, pp. 2894–2918.
https://doi.org/10.2514/1.J052525

[16] Solomon, J. T., Cairnes, K., Nayak, C., Jones, M., and Alexander, D., "Design and Characterization of Nozzle Injection Assemblies Integrated High-Frequency Microactuators," *AIAA Journal* Vol. 56, No. 9, pp. 3436–3448, 2018.
https://doi.org/10.2514/1.J056642

[17] Ali, M. Y., Arora, N., Topolski, M., Alvi, F. S., and Solomon, J. T., "Properties of Resonance Enhanced Microjets in Supersonic Crossflow," *AIAA Journal*, Vol. 55, No. 3, 2017, pp. 1075–1081. https://doi.org/10.2514/1.J055082

[18] Solomon, J. T., Kumar, R., and Alvi, F. S., "High-Bandwidth Pulsed Microactuators for High-Speed Flow Control," *AIAA Journal*, Vol. 48, No. 10, 2010, pp. 2386–2396. https://doi.org/10.2514/1.J050405

[19] Solomon, T., "High-Bandwidth Unsteady Actuators for Active Control of High-Speed Flows," Ph.D. Dissertation, Florida State Univ., 2010, http://purl.flvc.org/fsu/fd/FSU_migr_etd-1642.

[20] Lozano, A., Smith, S. H., Mungal, M. G., and Hanson, R. K., "Concentration Measurements in a Transverse Jet by Planar Laser-Induced Fluorescence of Acetone" *AIAA Journal*, Vol. 32, No. 1, 1994, pp. 218–221. https://doi.org/10.2514/3.11974

[21] Lozano, A., Yip, B., and Hanson, R. K., "Acetone: A by Planar Laser-Induced Fluorescence," *Experiments in Fluids*, Vol. 13, No. 6, 1992, pp. 369–376. https://doi.org/10.1007/BF00223244

B. M. Argrow
Associate Editor